RSC Advances

PAPER

Cite this: *RSC Adv.*, 2022, **12**, 22492

Role of composition and texture on bifunctional catalytic performance of extruded Au–Cu alloys†

Kechang Shen, *[a] Qingtao Gong,[a] Hao Zhang,[b] Kangqiang Li,[a] Zhongyu Sun,[a] Guihua Li,[c] Xin Hu,[d] Lu Liu[e] and Weimin Wang *[b]

Received 2nd June 2022
Accepted 25th July 2022

DOI: 10.1039/d2ra03438g

rsc.li/rsc-advances

The catalytic activity of Au_2Cu and AuCu samples for the electro-oxidation of CH_3OH and HCOOH, together with their structure and micro-hardness were investigated using various techniques. The addition of Cu can improve the micro-hardness of samples, which is ascribed to the solid solution strengthening effect. The Schmid factor and low angle grain boundary fraction confirm the difference of plastic deformation ability for samples, being consistent with hardness results. The Au–Cu samples exhibit good bifunctional catalytic performance due to the synergistic effect between Au and Cu. In addition, the Au_2Cu sample exhibits a higher catalytic activity than the AuCu sample, suggesting that appropriate preferred orientation plays a key role in the improvement of catalytic activities of Au based catalysts.

1. Introduction

Au is a noble metal which once was thought to be inactive due to its full 5d band structure and high ionization potential.[1,2] However, since the beginning of the 20th century, this view has gradually been changed. As early as 1906, Bone and Wheeler found that the reaction of hydrogen and oxygen can be catalyzed by Au under certain conditions.[3] In 1973, Bond *et al.* reported the catalytic activity of Au for ethylene hydrogenation.[4] In 1985, Hutchings reported that Au also exhibited good catalytic activity for the hydrochlorination of acetylene.[5] In 1987, Haruta *et al.* first found that Au exhibited high catalytic activity for the oxidation of CO at low temperature.[6,7] Based on these studies, the catalytic activity of Au has been confirmed continuously.

With the consumption of fossil fuels, the demand for clean energy increases. Due to significant potential applications for electric vehicles, distributed home power generators, and power sources for small and portable electronics, fuel cells can contribute to solving the global energy crisis.[8] It is necessary to decrease the cost and improve the oxidation kinetics of Au based catalysts for the development of fuel cells. However, active site density and intrinsic activity define the efficiency of catalyst, and active sites play important role in understanding of catalytic mechanism and driving the development of catalyst.[9,10] Alloying noble metals with non-noble metals is a promising method to obtain catalysts with reduced cost and more active sites, which is helpful for the improvement of catalytic activity.[11] In fact, bimetallic catalysts usually exhibit superior performance than monometallic catalysts, which is ascribed to the synergistic effect between Au and alloying element.[12–14] The electro-oxidation reactions of methanol (CH_3OH) and formic acid (HCOOH) play the important roles in the development of direct methanol fuel cells (DMFCs) and direct formic acid fuel cells (DFAFCs).[15,16] Recently, there are some bimetallic catalysts used for DMFCs and DFAFCs. For example, Kim *et al.* prepared carbon-supported Pt–Ru catalyst with excellent catalytic activity for oxidation of CH_3OH and improved the fuel cell performance;[17] Lu *et al.* prepared Pd–Cu nanocrystals which exhibited high catalytic activity for the oxidation of HCOOH.[18]

It is considered that Au–Cu alloy catalyst may also potentially act as promising alternative for the electro-oxidation reactions of CH_3OH and HCOOH. In recent years, Au–Cu alloys have attracted many attentions due to the improved catalytic activity for some reactions and the low cost of Cu.[19–21] For example, Bauer *et al.* reported that silica supported AuCu alloy catalyst showed a good catalytic activity for CO oxidation;[1] Zhang *et al.* reported that $AuCu_3$/C intermetallic nanoparticles exhibited a better catalytic activity for the oxygen reduction reactions in alkaline solution;[22] Schünemann *et al.* reported that due to the synergistic effect between Au and Cu, the mesoporous silica supported AuCu nanoparticles exhibited a better catalytic activity for the glycerol oxidation;[23] Birhanu *et al.* reported that Au–Cu bimetallic nanoparticles exhibited a good catalytic

[a]Ulsan Ship and Ocean College, Ludong University, Yantai 264025, China. E-mail: kechangshen@ldu.edu.cn

[b]Key Laboratory for Liquid-Solid Structural Evolution and Processing of Materials, Ministry of Education, Shandong University, Jinan 250061, China. E-mail: weiminw@sdu.edu.cn

[c]Shandong Institute of Metrology, Jinan 250014, China

[d]School of Mathematics and Statistics Science, Ludong University, Yantai 264025, China

[e]College of Transportation, Ludong University, Yantai 264025, China

† Electronic supplementary information (ESI) available. See https://doi.org/10.1039/d2ra03438g

activity for the electrochemical reduction reaction of CO_2.[24] These Au–Cu catalysts are all in nanoscale and their catalytic activity are expected to be improved based on the adjustment of size and supporter. However, the study on catalytic activity of Au–Cu alloy catalysts for the electro-oxidation reactions of CH_3OH and HCOOH is few. Hence, the bifunctional catalytic performance of Au–Cu alloys is valuable to be investigated.

For a long time, it has been found that texture (preferred orientation) can affect the performance of Au catalysts.[25–27] Therefore, the catalytic activity of Au–Cu alloy catalyst may be improved based on the regulation of composition and texture. This work investigated the extruded Au–Cu alloy plates which may exhibit a certain texture, in order to find out the effect of composition and texture on the structure, micro-hardness and catalytic activity. It is expected that the valuable suggestions can be put forward for improving the catalytic activity of Au based alloy catalysts.

2. Experimental methods

The Au_2Cu and AuCu alloys employed in this study were prepared using a mini electric arc furnace (MAM-1, Edmund Bühler GmbH) under an Ar atmosphere. The compositions of samples are shown in Table 1. In order to ensure that the ingots can have a uniform structure, the pure Au and Cu were smelted in water-cooled copper mould of the arc furnace for 3 times (smelting temperature: 2500 °C, smelting time: 15 s, cooling time: 5 min). Then the original spherical ingots were extruded into thin plates with a thickness of 0.3 mm using a tablet press, therefore, the tested samples are in extruded state.

The phase compositions of samples were measured using X-ray diffractometer (XRD, Rigaku D/MAX-2500/PC) with a Cu target (Cu Kα, $\lambda = 0.154056$ nm). Based on the XRD data, the lattice constant a_0 is calculated according to extended Bragg equation.[28]

$$a_0 = \frac{\lambda}{2\sin\theta}\sqrt{h^2 + k^2 + l^2} \quad (1)$$

where λ is the radiation wavelength, θ is the diffraction angle, and (h, k, l) is the crystal plane index.

The surface morphologies of samples and EDS mapping were observed using scanning electron microscopy (SEM, SU-70 and JSM-7610F). In order to investigate the element valence states and electronic structure of sample surfaces, the X-ray photoelectron spectroscopy (XPS, Escalab 250Xi) with Al-α radiation was used. The binding energies of tested elements for XPS test were calibrated by carbon contamination with C 1s peak (284.8 eV).

The texture changes of Au_2Cu and AuCu samples were explored using electron backscatter diffraction (EBSD, equipped with the Hitachi S-3400N SEM). Before the EBSD test, the samples were ion etched (voltage: 6 kV, incident angle: 8°, time: 45 min). The Schmid factor (SF), grain diameter, misorientation angle distribution, orientation maps and pole figures can be obtained using the software of HKL Channel 5.

The micro-hardness of samples was tested using HVT-1000A digital display micro-hardness tester. During the test, the applied load is 0.2 kg and the holding time is 15 s. Each sample was tested for 10 times and the average value is taken.

The cyclic voltammogram (CV) curves in 0.5 M KOH + 0.5 M CH_3OH solution (reference electrode in alkaline electrolyte: $Hg|HgO|OH^-$, MOE) and 0.5 M H_2SO_4 + 0.5 M HCOOH solution (reference electrode in acid electrolyte: $Hg|Hg_2SO_4|SO_4^{2-}$, MSE) were measured using advanced electrochemical workstation (CHI660E, Shanghai Chenhua Instrument Co. Ltd.). The CV curves were scanned initially from negative to positive potential during the test process.

Table 1 Composition of Au_2Cu and AuCu samples

Samples	Au (wt%)	Cu (wt%)
Au_2Cu	87.50	12.50
AuCu	75.00	25.00

3. Result and discussion

3.1 Structure and micro-hardness of samples

It is known that Au and Cu can form solid solution, and order–disorder transformation can occur with the change of temperature.[29,30] Fig. 1 shows the XRD patterns of Au_2Cu and AuCu samples, together with their appearances. There are five peaks on the XRD patterns which are indexed to the (111), (200), (220), (311) and (222) crystal planes of Au. The surface morphologies of two samples and the corresponding EDS mapping results are shown in Fig. S1.† It can be found that original sample surfaces are relatively smooth, and Au and Cu elements are uniformly distributed on the sample surfaces (Fig. S1(a)–(c) and (e)–(g)†). In addition, the compositions of two samples are basically

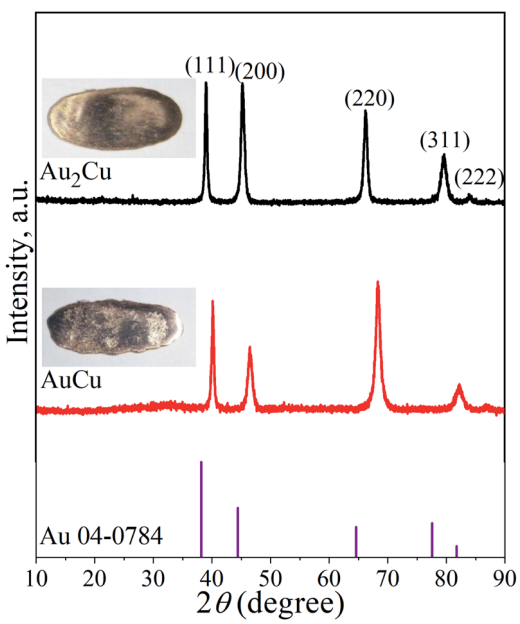

Fig. 1 XRD patterns of Au_2Cu and AuCu samples as well as the standard XRD pattern of pure Au. The inserts are the corresponding appearances of tested samples.

Table 2 Diffraction peak positions (2θ) of XRD patterns

Samples	(111)	(200)	(220)	(311)	(222)
Pure Au	38.184°	44.392°	64.576°	77.547°	81.721°
Au_2Cu	39.042°	45.281°	66.261°	79.662°	84.017°
AuCu	40.162°	46.540°	68.342°	82.280°	86.980°

consistent with the designed compositions (Fig. S1(d), (h)† and Table 1). Based on the XRD and EDS mapping results, it is believed that both samples are composed of Au–Cu solid solutions.

As shown in Table 2, compared to the diffraction peak position (2θ) of standard Au, the 2θ of Au–Cu samples shifts toward the higher value with the increase of Cu content. According to the extended Bragg equation (eqn (1)), a higher 2θ means a lower a_0. Since the atomic radius of Au and Cu respectively are 1.442 Å and 1.278 Å, the increase of Cu content can lead to a larger contraction of lattice structure of solid solution.[22]

Since the as-cast samples were extruded into plates in order to obtain a certain texture, the mechanical property which can affect the extrusion process is necessary to be investigated. It is believed that the mechanical property results can provide some clues for improving catalytic activities of samples based on texture regulation in future. Fig. 2 shows the micro-hardness of samples. It can be found that the micro-hardness of Au–Cu samples (Au_2Cu: 204.2 $HV_{0.2}$, AuCu: 275.4 $HV_{0.2}$) is higher than that of pure Au (33.8 $HV_{0.2}$) apparently, and the increase of Cu content is benefit for the enhancement of micro-hardness of Au–Cu samples. In addition, the Schmid factor (SF) can be assessed using EBSD analysis based on Schmid law. Schmid law states that a slip system can be activated if the resolved shear stress (τ) on the slip plane and in the slip direction reaches a certain critical value. The τ in the slip direction can be expressed as the following equation.[31,32]

$$\tau = \frac{F}{A}\cos\lambda\cdot\cos\varphi \quad (2)$$

Here, F and A respectively are the loading force and the section area of sample (*i.e.*, $\frac{F}{A}$ is stress), λ is the angle between stress axis and the slip direction, and φ is the angle between stress axis and the normal direction of the slip plane. The SF is defined as $\cos\lambda\cdot\cos\varphi$. Hence, a higher SF means a higher plastic deformation tendency. As shown in Fig. 3, the SF of AuCu sample is lower than that of Au_2Cu sample, which is consistent with the micro-hardness results.

As mentioned above, there is the lattice distortion in the Au–Cu solid solution, which can lead to the solid solution strengthening effect. As shown in Fig. 4, although the average grain diameter for AuCu sample (~13.37 μm) is slightly higher than that for Au_2Cu sample (~12.35 μm), the AuCu sample with a larger lattice distortion exhibits a higher micro-hardness value.

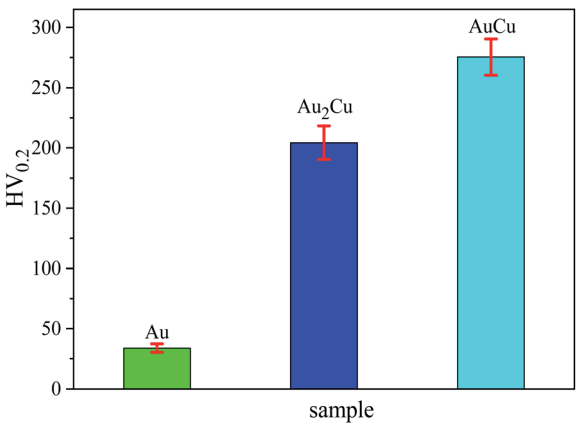

Fig. 2 Micro-hardness of Au_2Cu and AuCu samples. Red line segment represents the error bar.

3.2 Electro-oxidation reaction of CH_3OH on Au–Cu samples

Fig. 5 shows the CV curves of Au–Cu samples in 0.5 M KOH + 0.5 M CH_3OH solution (scan rate v: 50 mV s^{-1}). As the potential sweeps positively, there are the peaks P_1 (~−0.01 V *vs.* MOE), P_2 (~0.36 V *vs.* MOE), P_3 (~0.57 V *vs.* MOE) and P_4 (~0.99 V *vs.*

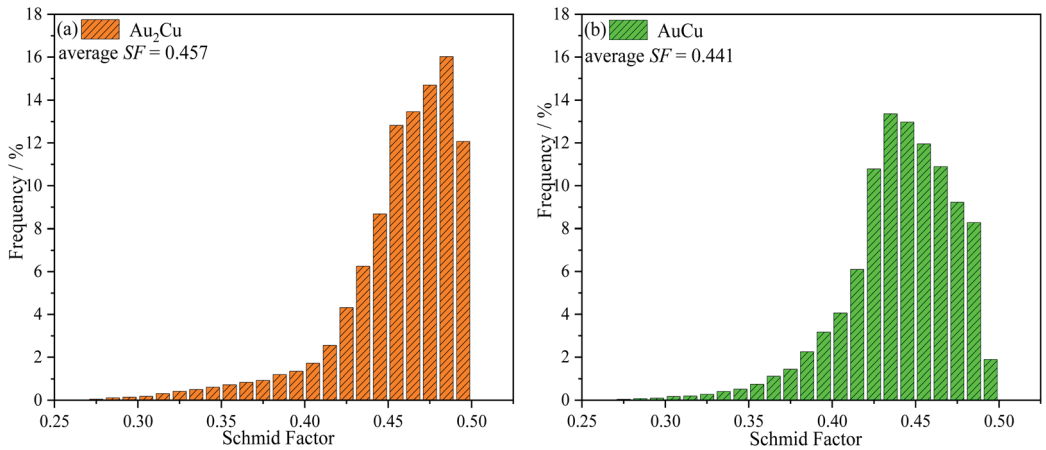

Fig. 3 Schmid factors (SF) of Au_2Cu and AuCu samples.

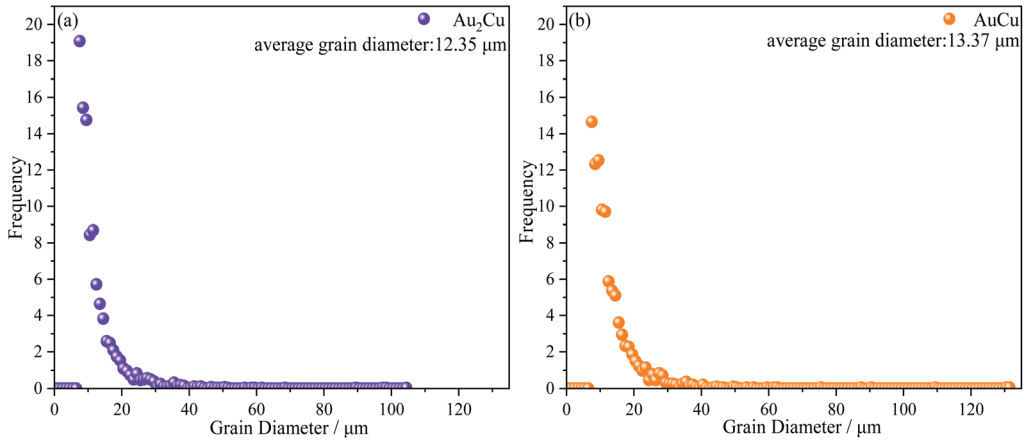

Fig. 4 Grain diameter distribution of Au_2Cu and AuCu samples.

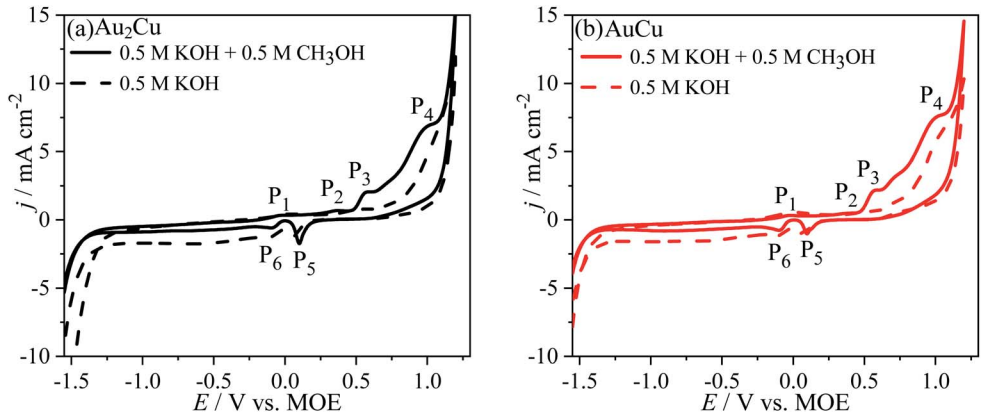

Fig. 5 Cyclic voltammograms (CVs) of (a) Au_2Cu and (b) AuCu samples in 0.5 M KOH + 0.5 M CH_3OH solution. The dash lines are the CV curves in 0.5 M KOH solution. Scan rate *v*: 50 mV s^{-1}.

MOE). The peak P_1 is corresponding to the partial charge-transfer of chemisorbed OH^- anions, pre-oxidation of Au surface and formation of pre-oxidation precursor.[26,33]

$$Au + OH^- - \lambda e^- \rightarrow Au\text{–}OH_{ads}{}^{(1-\lambda)-} \quad (3)$$

Here ads indicates the chemisorbed species on Au surface and λ varies from 0 to 1. The chemisorbed species can play a promoting role in the electro-oxidation of CH_3OH in alkaline solution.[33] The peak P_2 can be assigned to the formation of Cu(I) species.[34,35] As shown in Fig. S2,† the peaks P_3 and P_4 also appear on the CV curves for pure Au. The current density (*j*) of peak P_3 in 0.5 M KOH + 0.5 M CH_3OH solution is apparently higher than that in 0.5 M KOH solution, indicating that the peak P_3 can be ascribed to the oxidation of Au and CH_3OH. In addition, it is thought that the peak P_3 for Au–Cu samples should be also related to the formation of Cu(II) species.[34,35] In this region, CH_3OH is oxidized to $HCOO^-$ with a reaction of 4 electron transfer.[33,36]

$$Au\text{–}OH_{ads}{}^{(1-\lambda)-} + OH^- - (2-\lambda)e^- \rightarrow AuO + H_2O \quad (4)$$

$$CH_3OH + 5OH^- - 4e^- \rightarrow HCOO^- + 4H_2O \quad (5)$$

The peak P_4 for Au–Cu samples is apparently higher than that for pure Au. It is thought that the peak P_4 can be ascribed to the oxidation reaction of Cu(II) to Cu(III), which is accompanied by the oxidation of CH_3OH on Au oxide and Cu(III) species surfaces. In fact, Cu(III) species is a strong oxidant which can play an important role in the oxidation of CH_3OH, and after the reaction the Cu(III) will be reduced to Cu(II).[34,35] During this reaction process, the CH_3OH is oxidized to $CO_3{}^{2-}$ with a reaction of 6 electron transfer.[26,33]

$$CH_3OH + 8OH^- - 6e^- \rightarrow CO_3{}^{2-} + 6H_2O \quad (6)$$

As the potential sweeps negatively, there is the peak P_5 (~0.10 V *vs.* MOE) ascribed to the reduction reaction of Au oxides and Cu(II) species, while the peak P_6 (~−0.09 V *vs.* MOE) can be assigned to the reduction of Cu(I) to Cu.

However, it can be found that the *j* of peaks P_3 and P_4 for Au–Cu samples are obviously higher than that for pure Au (Fig. 5 and S2†), indicating that the addition of Cu is benefit for

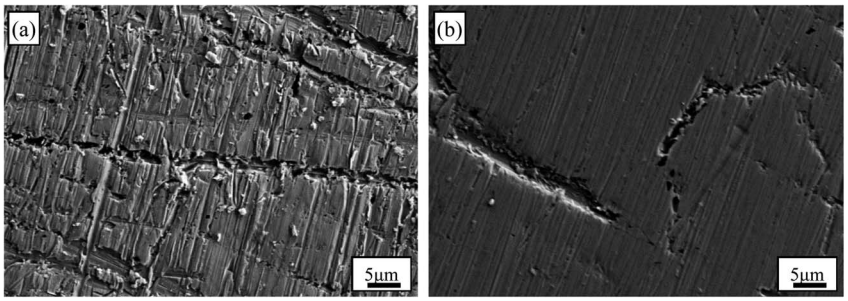

Fig. 6 SEM images of (a) Au_2Cu and (b) AuCu samples after CV tests in 0.5 M KOH + 0.5 M CH_3OH solution.

enhancing the catalytic activity of Au based catalysts for the electro-oxidation of CH_3OH. The improvement of catalytic activity is related to the synergistic effect between Au and Cu.[12,23]

The SEM images of Au–Cu sample surfaces after CV tests in 0.5 M KOH + 0.5 M CH_3OH solution are shown Fig. 6. The surfaces of Au–Cu samples after test are much rougher compared with those before test (Fig. S1† and 6). In addition, the surface of Au_2Cu sample is rougher than that of AuCu sample, indicating that the redox reactions for Au_2Cu sample are more intense than those for AuCu sample. However, the surface of pure Au sample is relatively smooth after CV test (Fig. S3†), also meaning the higher activity for Au–Cu samples. The EDS mapping results of Au–Cu samples after CV test are shown in Fig. S4.† It is clear that compared with the Cu contents of two sample surfaces before CV test, the Cu contents after CV test decrease, indicating that partial Cu was released from the surface into the solution during the reaction process (Fig. S1 and S4†).

According to ref. 37 and 38, the relationship between j and v can be expressed as following.

$$\log j = b \log v + a \tag{7}$$

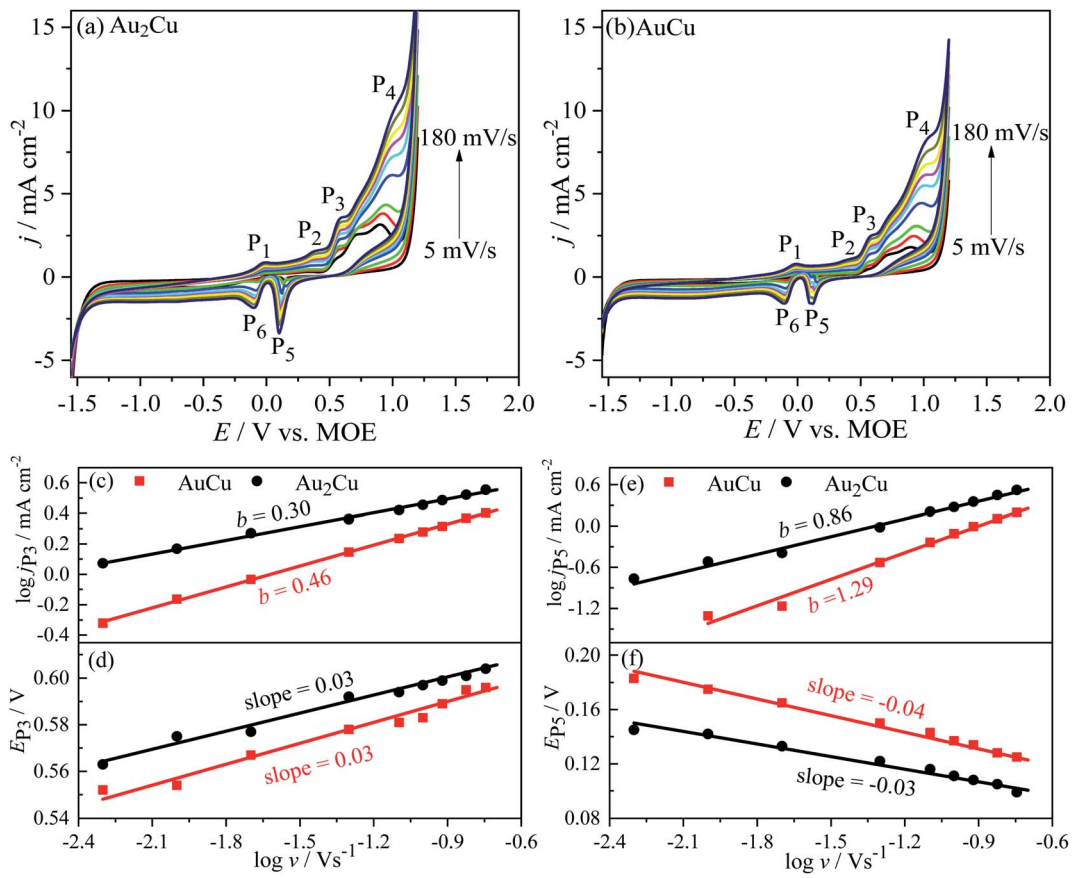

Fig. 7 Cyclic voltammograms (CVs) of (a) Au_2Cu and (b) AuCu samples in 0.5 M KOH + 0.5 M CH_3OH solution with different scan rates (scan rate v: 5, 10, 20, 50, 80, 100, 120, 150 and 180 mV s^{-1}). The dependency of the log of current densities log j and the potentials E of (c and d) peak P_3 and (e and f) peak P_5 of CV curves in (a) and (b) on log v are also shown.

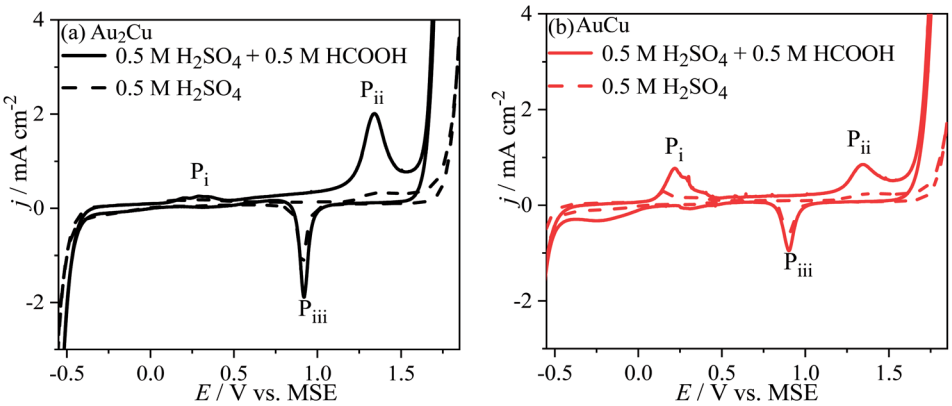

Fig. 8 Cyclic voltammograms (CVs) of (a) Au_2Cu and (b) AuCu samples in 0.5 M H_2SO_4 + 0.5 M HCOOH solution. The dash lines are the CV curves in 0.5 M H_2SO_4 solution. Scan rate v: 50 mV s^{-1}.

Here, a and b are the adjustable constants. The b value corresponded to the slope of fitted line can indicate the adsorption-controlled process ($b = 1.0$) and diffusion-controlled ($b = 0.5$) process, respectively.[39–41] Fig. 7 shows the CV curves of Au–Cu samples with different v in 0.5 M KOH + 0.5 M CH_3OH solution. The j increases with increasing the v, because the concentration gradient becomes much steeper in diffusion layer (Fig. 7(a) and (b)).[42] According to the log j–log v plots, the b values of j_{P_3} are 0.30 and 0.46 for Au_2Cu and AuCu respectively (Fig. 7(c)). Hence, it is believed that the oxidation reaction corresponded to peak P_3 is mainly controlled by diffusion. However, there is small deviation from the theoretical value of 0.5, which is related with the kinetic limitation in reaction.[39,40] The b values corresponded to j_{P_5} are 0.86 and 1.29 for Au_2Cu and AuCu respectively (Fig. 7(e)), indicating that the reduction reactions corresponded to peak P_5 mainly are adsorption-controlled processes. With increasing the v, the peak-to-peak potential separation ($\Delta E_P = E_{P_3} - E_{P_5}$) increases (Fig. 7(d) and (f)), which is due to the presence of kinetic limitation.[40,43]

3.3 Electro-oxidation reaction of HCOOH on Au–Cu samples

It is known that the electro-oxidation reaction of HCOOH can proceed *via* direct pathway and indirect pathway.[44,45]

$$HCOOH \rightarrow CO_2 + 2H^+ + 2e^- \quad (8)$$

$$HCOOH \rightarrow CO_{ads} + H_2O \rightarrow CO_2 + 2H^+ + 2e^- \quad (9)$$

The direct pathway is dehydrogenation reaction during which CO_2 is directly formed (eqn (8)). The indirect pathway is dehydration reaction, during this reaction process CO_{ads} can be formed and then it is oxidized to CO_2 at a higher potential (eqn (9)).

Fig. 8 shows the CV curves of Au–Cu samples in 0.5 M H_2SO_4 + 0.5 M HCOOH solution. There are peaks P_i, P_{ii} and P_{iii} on the CV curves, while there is no peak P_i for pure Au (Fig. S5†). Hence, the peak P_i should be related with Cu. In addition, the j of peaks P_i and P_{ii} on CV curve in solution contained HCOOH is apparently higher than those only in H_2SO_4 solution. Hence, the peak P_i can be ascribed to the oxidation reactions of Cu and HCOOH, and the peak P_{ii} can be ascribed to the oxidation reactions of Au and HCOOH. Furthermore, the j of peak P_{ii} for Au–Cu samples is higher than that for pure Au, indicating that the addition of Cu also can improve the catalytic activity of Au based catalyst for electro-oxidation of HCOOH (Fig. 8 and S5†). Here, it is thought that the electro-oxidation of HCOOH proceeds *via* direct pathway (eqn (8)). In the negative scans of CV curves, there is a peak P_{iii} ascribed to the reduction reaction of Au and Cu oxides.

Since the peak P_i is related to Cu, therefore increasing the Cu content, the j of peak P_i increases. Consequently, there are more Cu oxides formed on the surface of AuCu sample than those of

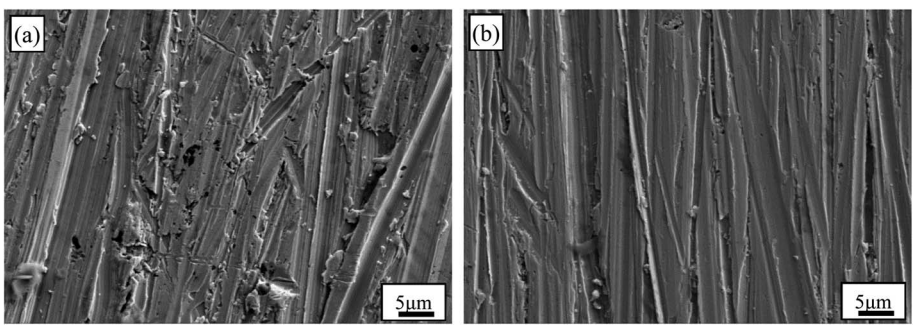

Fig. 9 SEM images of (a) Au_2Cu and (b) AuCu samples after CV tests in 0.5 M H_2SO_4 + 0.5 M HCOOH solution.

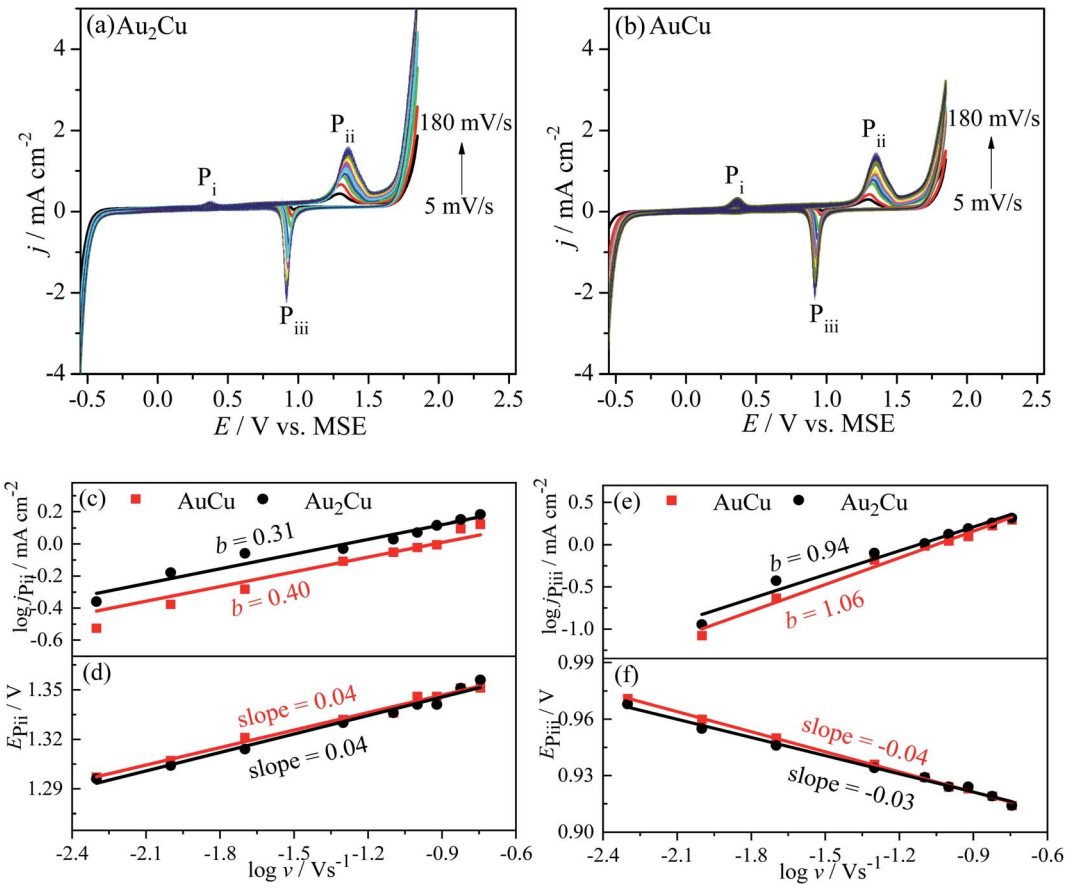

Fig. 10 Cyclic voltammograms (CVs) of (a) Au_2Cu and (b) AuCu samples in 0.5 M H_2SO_4 + 0.5 M HCOOH solution with different scan rates (scan rate *v*: 5, 10, 20, 50, 80, 100, 120, 150 and 180 mV s^{-1}). The dependency of the log of current densities log *j* and the potentials *E* of (c and d) peak P_{ii} and (e and f) peak P_{iii} of CV curves in (a) and (b) on log *v* are also shown.

Au_2Cu sample. Because the formed Cu oxides can isolate the active sites from catalyzing the electro-oxidation reaction of HCOOH, the *j* of peak P_{ii} for AuCu sample is lower than that for Au_2Cu sample (Fig. 8).

The surface morphologies of Au–Cu samples after CV tests in 0.5 M H_2SO_4 + 0.5 M HCOOH solution are shown in Fig. 9. The surfaces of Au–Cu samples after test are much rougher than those before test (Fig. S1† and 9). It can also be seen that the surface of pure Au after CV test is relatively smooth, while the surfaces of Au–Cu samples are much rougher (Fig. 9 and S6†), also indicating a higher catalytic activity of Au–Cu samples.

Fig. 10 shows the CV curves of Au–Cu samples with different *v* in 0.5 M H_2SO_4 + 0.5 M HCOOH solution. It is similar to the case in CH_3OH solution, the *j* increases with increasing the *v* (Fig. 10(a) and (b)), which is due to the steepening of concentration gradient in diffusion layer.[42] According to the log *j*–log *v* plots, the *b* values for peak P_{ii} of Au_2Cu and AuCu samples are 0.31 and 0.40 respectively, while the *b* values for peak P_{iii} of two samples respectively are 0.94 and 1.06 (Fig. 10(c) and (e)). Hence, it is considered that the oxidation reactions corresponded to peak P_{ii} are mainly controlled by diffusion together with the presence of kinetic limitation, and the reduction reactions corresponded to peak P_{iii} are mainly controlled by adsorption. With increasing the *v*, the oxidation peak potentials ($E_{P_{ii}}$) shift to the positive direction (Fig. 10(d)), while the potentials of reduction peaks ($E_{P_{iii}}$) shift to the negative direction (Fig. 10(f)), resulting in an increase of peak-to-peak potential separation ($\Delta E_P = E_{P_{ii}} - E_{P_{iii}}$). This increase also indicates the presence of kinetic limitation,[43] which is similar to the phenomenon in CH_3OH solution (Fig. 7(d) and (f)).

3.4 Effect of alloying and texture on catalytic activity of Au–Cu samples

As mentioned above, the alloying of Au with Cu is benefit for the improvement of catalytic activity of Au based catalysts for both electro-oxidation reactions of CH_3OH and HCOOH, and the Au_2Cu sample exhibits a better catalytic activity than AuCu sample (Fig. 7 and 10).

In fact, the alloying can tune the electronic structure of Au based catalysts, which plays a key role in catalytic activity.[46,47] As shown in Fig. 11 and S7,† the XPS spectra of Au_2Cu and Au sample surfaces before and after the appearance of peak P_3 on CV curves tested in 0.5 M KOH + 0.5 M CH_3OH solution were obtained. It can be found that the binding energies (BE) of Au 4f and Cu 2p tend to shift towards for the higher values after the peak P_3. According to the BE, there is zero valent Au (Au^0) on the

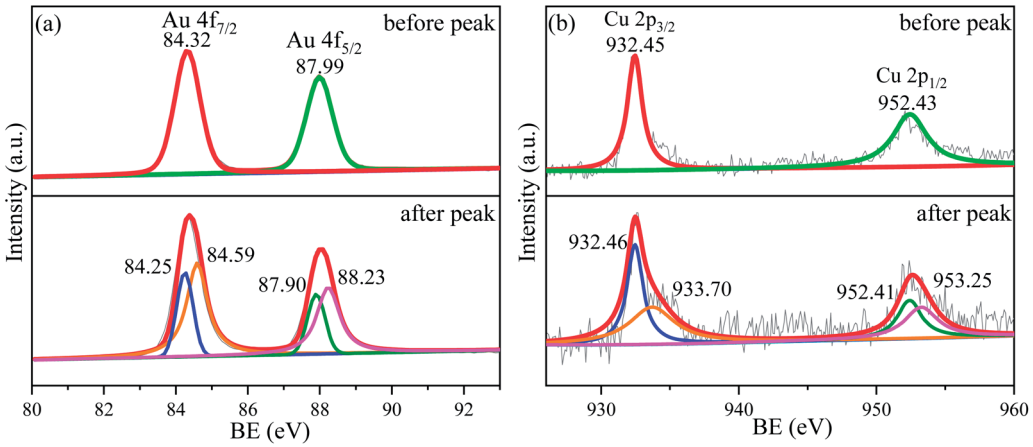

Fig. 11 XPS spectra for (a) Au 4f and (b) Cu 2p of sample surfaces with Au_2Cu before and after the anodic peak P_3 of CV curves tested in 0.5 M KOH + 0.5 M CH_3OH solution.

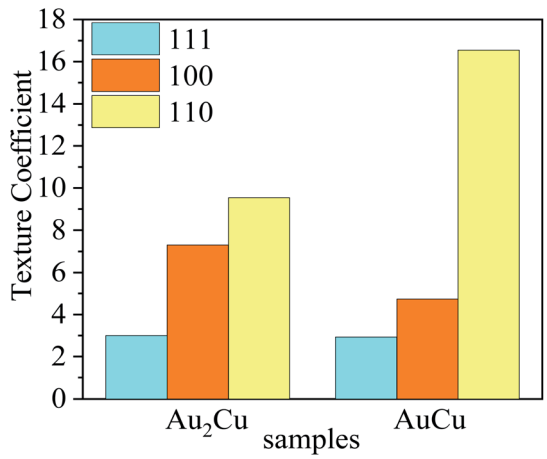

Fig. 12 Texture coefficients (TC) of (111), (100) and (110) crystal planes for Au_2Cu and AuCu samples.

Au_2Cu and Au sample surfaces before the peak P_3, while the electronic structure of Au 4f after the peak P_3 can be considered as coexistence of Au^0 and Au^+ (Fig. 11(a) and S7†).[48] However, the BE of Au $4f_{7/2}$ and Au $4f_{5/2}$ for Au^0 on Au_2Cu sample surface (before the peak P_3: 84.32 eV and 87.99 eV; after the peak P_3: 84.25 eV and 87.90 eV) were higher than those on Au sample surface (before the peak P_3: 84.16 eV and 87.83 eV; after the peak P_3: 84.14 eV and 87.82 eV), indicating that Au tends to lose valence electrons to Cu and this perturbation can affect the surface energy of Au to achieve a better electrochemical performance.[12,24] In addition, the BE of Cu 2p before the peak P_3 are ascribed to Cu^+, while those after the peak P_3 are ascribed to Cu^+ and Cu^{2+} (Fig. 11(b)).[49–51] In fact, compared with pure Au, the alloying with Cu can lead to the upper shift of d-band center, which can enhance the combine ability with O for alloys.[46,52,53] Moreover, Cu can form Cu–O species which can provide reactive O during the oxidation process.[14,49] Hence, the Au–Cu samples exhibit a better catalytic activity than monometallic Au.

According to ref. 27, 54 and 55, preferred orientation plays a key role in catalytic activity of Au based catalysts. Since the Au–Cu samples are in extruded state, the difference of catalytic activity between Au_2Cu and AuCu samples may be related with their texture. The degree of crystalline orientation can be determined using texture coefficient (TC).[56,57]

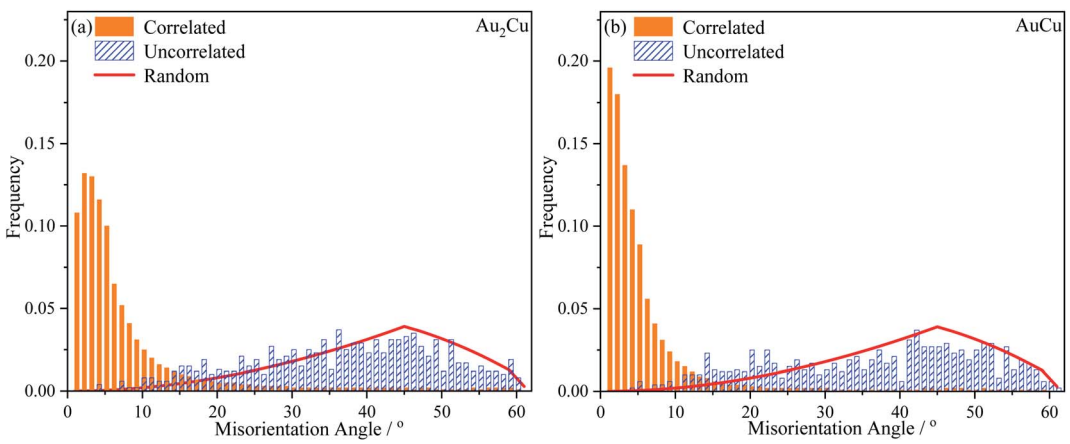

Fig. 13 Histograms of misorientation angle distributions of (a) Au_2Cu and (b) AuCu samples.

Table 3 Fractions of low angle grain boundary (LAGB), medium angle grain boundary (MAGB) and high angle grain boundary (HAGB) for Au_2Cu and AuCu samples

Samples	LAGB	MAGB	HAGB
Au_2Cu	0.49	0.36	0.15
AuCu	0.61	0.29	0.10

$$TC_{(hkl)_i} = \frac{I_{(hkl)_i}/I_{0(hkl)_i}}{\frac{1}{n}\sum_{i=1}^{n}\frac{I_{(hkl)_n}}{I_{0(hkl)_n}}} \quad (10)$$

where $I_{(hkl)_i}$ and $I_{0(hkl)_i}$ are the integral intensities of $(hkl)_i$ diffraction peaks for the experimental and completely random samples, respectively; n is the number of diffraction peaks considered in the analysis. It can be seen from Fig. 12 that the TC values of (111) crystal planes for both samples are nearly equal, while the TC value of (100) crystal plane for Au_2Cu sample is much higher and its TC value of (110) crystal plane is much lower.

In order to further verify the texture variation, the misorientation angle distributions and pole figures for samples were obtained using EBSD technique. In Fig. 13, the "Correlated" misorientation angles are calculated from neighboring points, the "Uncorrelated" misorientation angles are calculated from random points, and the "Random" misorientation distribution is deduced from a completely random texture. It can be found that there are slight deviations between the uncorrelated misorientation and random misorientation for both Au–Cu samples, indicating the presence of weak texture. According to the correlated misorientation, the fractions of low angle grain boundary (LAGB, <5°), medium angle grain boundary (MAGB, 5°–15°) and high angle grain boundary (HAGB, >15°) are listed in Table 3. It is known that the LAGB is mainly composed of a series of dislocations.[58–60] The fraction of LAGB in AuCu sample is about 61%, while that in Au_2Cu sample is about 49%. That is to say that there are more dislocations in AuCu samples,

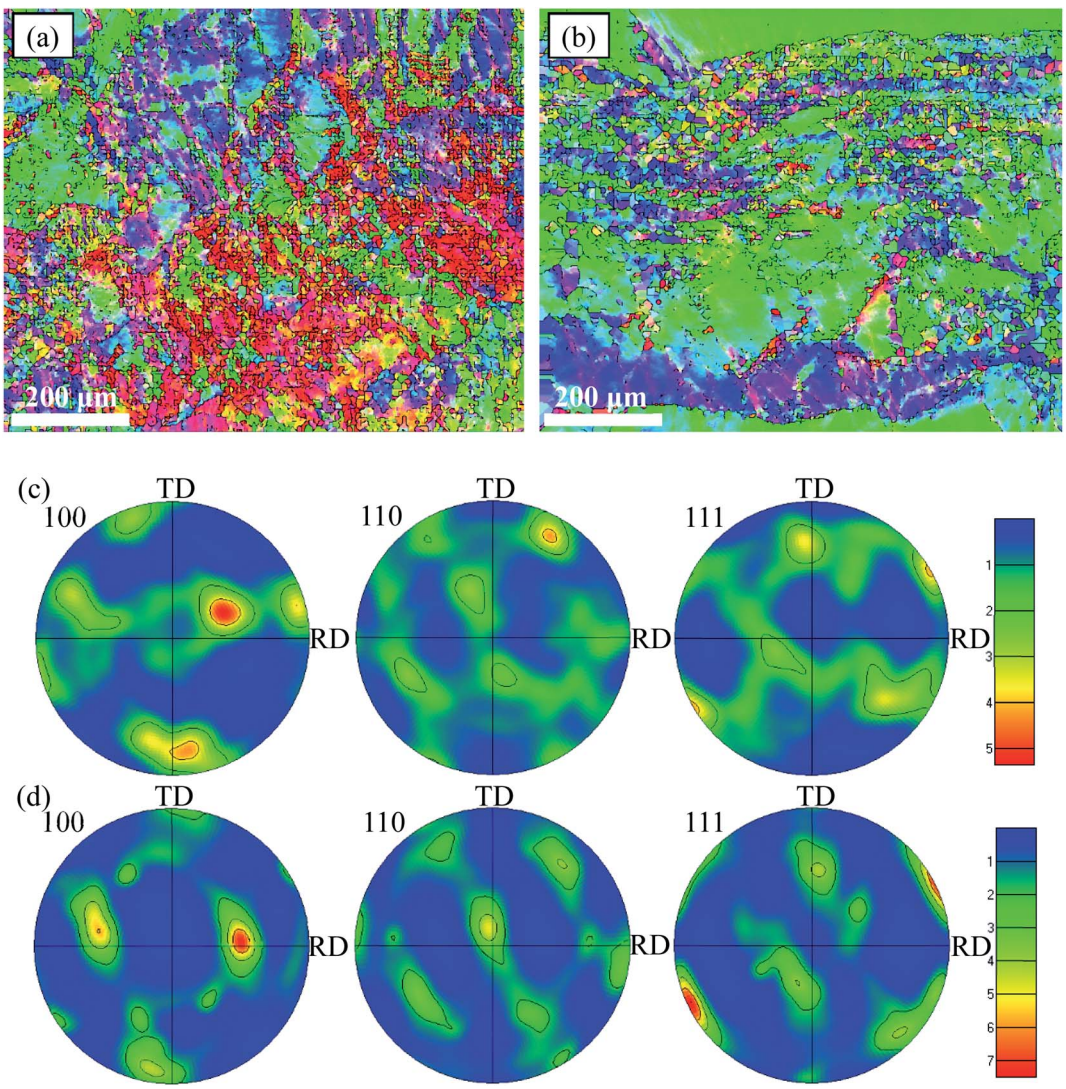

Fig. 14 Orientation maps of (a) Au_2Cu and (b) AuCu samples and pole figures of (c) Au_2Cu and (d) AuCu samples.

also indicating that the addition of Cu can affect the lattice structure of Au based catalysts and improve their plastic deformation ability.

The orientation maps and pole figures of Au–Cu samples are shown in Fig. 14. For the extruded samples, there are rolling direction (RD), transverse direction (TD) and normal direction (ND). The CV test surface is perpendicular to the ND of sample. It can be seen from the orientation maps that the grain size of AuCu sample is slightly larger than that of Au_2Cu sample, which is consistent with the grain diameter results (Fig. 4 and 14(a), (b)). According to pole figures, Au_2Cu sample exhibits a ⟨100⟩ preferred orientation (the normal direction of (100) crystal plane) which deviates about 30° from ND, while AuCu sample also exhibits a ⟨100⟩ preferred orientation which deviates about 50° from ND. Hence, compared with AuCu sample, more (100) crystal planes can be exposed on the CV test surface of Au_2Cu sample. It also can be found that AuCu sample exhibits an obvious ⟨110⟩ preferred orientation which is nearly parallel to the ND. In addition, both Au–Cu samples exhibit the ⟨111⟩ preferred orientations which deviate about 30° from RD. However, the pole figure results are consistent with the TC variation (Fig. 12 and 14(c), (d)). Based on the ref. 61, the interactions of Au(100) crystal plane and adsorbed O can lead to the drastic surface reconstruction, and the reconstructed Au(100) crystal plane exhibits a better catalytic activity. In fact, compared with Au(110) crystal plane, Au(100) crystal plane is considered to be more active for the catalytic reactions.[26,62,63] Hence, the Au_2Cu sample has a better catalytic activity than AuCu sample, which is ascribed to the different preferred orientations of their CV test surfaces.

4. Conclusions

Au_2Cu and AuCu samples were prepared using vacuum arc melting. Both samples are composed of Au–Cu solid solutions. A higher Cu content means a better solid solution strengthening effect. AuCu sample has a higher micro-hardness value than Au_2Cu sample, which is consistent with their plastic deformation ability confirmed by the SF values and fraction of LAGB.

The addition of Cu can improve the catalytic activity of Au based catalysts, which is related to the electron transfer between two elements and a better ability to combine with oxygen for Cu. There are more Au(100) crystal planes on the CV test surface of Au_2Cu sample. Since Au(100) crystal plane is more active for the catalytic reactions of Au based catalysts, hence Au_2Cu sample exhibits a better catalytic activity than AuCu sample. This work can provide a clue to tune the catalytic activity of Au based catalysts by alloying with Cu and obtaining appropriate preferred orientation.

Author contributions

Kechang Shen: methodology, investigation, writing – original draft, writing – review & editing. Qingtao Gong: funding acquisition. Hao Zhang: visualization. Kangqiang Li: visualization. Zhongyu Sun: supervision. Guihua Li: data curation, validation. Xin Hu: project administration. Lu Liu: formal analysis. Weimin Wang: funding acquisition, conceptualization, resources, writing – review & editing.

Conflicts of interest

The authors declare no competing interests.

Acknowledgements

This work was financially supported by National Natural Science Foundation of China (No. 51771103, 52101196 and 52171158), Key Research and Development Program of Shandong Province (No. 2021ZLGX01 and 2020ZLYS11), Major Innovation Projects in Shandong Province (No. 2020CXGC010701 and 2020CXGC010702), Yantai Science and Technology Planning Project (No. 2021ZDCX001), Open Project Program of Shandong Marine Aerospace Equipment Technological Innovation Center (Ludong University) (No. MAETIC2021-11), and Outstanding Youth Innovation Team Project of Shandong Higher Education Institution (No. 2021KJ042).

References

1 J. C. Bauer, D. R. Mullins, Y. Oyola, S. H. Overbury and S. Dai, *Catal. Lett.*, 2013, **143**, 926–935.
2 S. Kameoka and A. P. Tsai, *Catal. Lett.*, 2008, **121**, 337–341.
3 W. A. Bone and R. V. Wheeler, *Proc. R. Soc. A*, 1906, **77**, 146–147.
4 G. C. Bond, P. A. Sermon, G. Webb, D. A. Buchanan and P. B. Wells, *J. Chem. Soc., Chem. Commun.*, 1973, **13**, 444b–445b.
5 G. J. Hutchings, *J. Catal.*, 1985, **96**, 292–295.
6 M. Haruta, T. Kobayashi, H. Sano and N. Yamada, *Chem. Lett.*, 1987, **16**, 405–408.
7 X. Li, S. S. S. Fang, J. Teo, Y. L. Foo, A. Borgna, M. Lin and Z. Y. Zhong, *ACS Catal.*, 2012, **2**, 360–369.
8 B. Z. Fang, L. Daniel, A. Bonakdarpour, R. Govindarajan, J. Sharman and D. P. Wilkinson, *Small*, 2021, **17**, 2102288.
9 Z. P. Wang, B. B. Xiao, Z. P. Lin, Y. P. Xu, Y. Lin, F. Q. Meng, Q. H. Zhang, L. Gu, B. Z. Fang, S. J. Guo and W. W. Zhong, *Angew. Chem., Int. Ed.*, 2021, **60**, 23388–23393.
10 S. J. Shen, Z. Y. Hu, H. H. Zhang, K. Song, Z. P. Wang, Z. P. Lin, Q. H. Zhang, L. Gu and W. W. Zhong, *Angew. Chem., Int. Ed.*, 2022, **61**, e202206460.
11 Z. P. Lin, B. B. Xiao, M. Huang, L. H. Yan, Z. P. Wang, Y. C. Huang, S. J. Shen, Q. H. Zhang, L. Gu and W. W. Zhong, *Adv. Energy Mater.*, 2022, **12**, 2200855.
12 C. I. Oseghale, A. H. Abdalla, J. O. G. Posada and P. J. Hall, *Int. J. Hydrogen Energy*, 2016, **41**, 16394–16401.
13 K. C. Shen, G. H. Li, Q. Chen, L. C. Zhang and W. M. Wang, *J. Alloys Compd.*, 2020, **815**, 152409.
14 L. Ma, K. Laasonen and J. Akola, *J. Phys. Chem. C*, 2017, **121**, 10876–10886.
15 O. T. Ajenifujah, A. Nouralishahi, S. Carl, S. C. Eady, Z. Jiang and L. T. Thompson, *Chem. Eng. J.*, 2021, **406**, 126670.

16 D. M. Zhang, J. Du, J. Quinson and M. Arenz, *J. Power Sources*, 2022, **522**, 230979.
17 M. S. Kim, B. Z. Fang, N. K. Chaudhari, M. Song, T. S. Bae and J. S. Yu, *Electrochim. Acta*, 2010, **55**, 4543–4550.
18 L. F. Lu, B. Wang, D. Wu, S. H. Zou and B. Z. Fang, *Nanoscale*, 2021, **13**, 3709–3722.
19 Y. Sugano, Y. Shiraishi, D. Tsukamoto, S. Ichikawa, S. Tanaka and T. Hirai, *Angew. Chem., Int. Ed.*, 2013, **52**, 5295–5299.
20 L. Wolski, M. El-Roz, M. Daturi, G. Nowaczyk and M. Ziolek, *Appl. Catal., B*, 2019, **258**, 117978.
21 F. Du, H. M. Wang, X. Jin, W. A. Deng, C. Li, Z. X. Ren, H. Yan and B. Yin, *Catal. Lett.*, 2019, **149**, 1037–1045.
22 N. L. Zhang, X. Chen, Y. J. Lu, L. An, X. Li, D. G. Xia, Z. Zhang and J. X. Li, *Small*, 2014, **10**, 2662–2669.
23 S. Schünemann, G. Dodekatos and H. Tüysüz, *Chem. Mater.*, 2015, **27**, 7743–7750.
24 M. K. Birhanu, M. C. Tsai, C. T. Chen, A. W. Kahsay, T. S. Zeleke, K. B. Ibrahim, C. J. Huang, Y. F. Liao, W. N. Su and B. J. Hwang, *Electrochim. Acta*, 2020, **356**, 136756.
25 A. Hamelin, *J. Electroanal. Chem.*, 1996, **407**, 1–11.
26 Z. Borkowska, A. Tymosiak-Zielinska and G. Shul, *Electrochim. Acta*, 2004, **49**, 1209–1220.
27 C. L. Li, B. Jiang, H. R. Chen, M. Imura, L. W. Sang, V. Malgras, Y. Bando, T. Ahamad, S. M. Alshehri, S. Tominaka and Y. Yamauchi, *Nano Res.*, 2016, **9**, 1752–1762.
28 Y. Zhou and G. H. Wu, *Materials analysis and testing technology*, Harbin Institute of Technology Publisher, Harbin, 2007.
29 S. Kameoka and A. P. Tsai, *Catal. Today*, 2008, **132**, 88–92.
30 D. Kim, C. L. Xie, N. Becknell, Y. Yu, M. Karamad, K. Chan, E. J. Crumlin, J. K. Nørskov and P. D. Yang, *J. Am. Chem. Soc.*, 2017, **139**, 8329–8336.
31 D. B. Xia, X. Chen, G. S. Huang, B. Jiang, A. T. Tang, H. Yang, S. Gavras, Y. D. Huang, N. Hort and F. S. Pan, *Scr. Mater.*, 2019, **171**, 31–35.
32 T. Teshima, M. Kosaka, K. Ushioda, N. Koga and N. Nakada, *Mater. Sci. Eng., A*, 2017, **679**, 223–229.
33 J. T. Zhang, P. P. Liu, H. Y. Ma and Y. Ding, *J. Phys. Chem. C*, 2007, **111**, 10382–10388.
34 H. Heli, M. Jafarian, M. G. Mahjani and F. Gobal, *Electrochim. Acta*, 2004, **49**, 4999–5006.
35 G. W. Wang, L. Xiao, B. Huang, Z. D. Ren, X. Tang, L. Zhuang and J. T. Lu, *J. Mater. Chem.*, 2012, **22**, 15769–15774.
36 H. Xu, K. C. Shen, S. Liu, L. C. Zhang, X. G. Wang, J. Y. Qin and W. M. Wang, *J. Phys. Chem. C*, 2018, **122**, 3371–3385.
37 I. E. Rauda, V. Augustyn, B. Dunn and S. H. Tolbert, *Acc. Chem. Res.*, 2013, **46**, 1113–1124.
38 V. Augustyn, J. Come, M. A. Lowe, J. W. Kim, P. L. Taberna, S. H. Tolbert, H. D. Abruña, P. Simon and B. Dunn, *Nat. Mater.*, 2013, **12**, 518–522.
39 A. Velázquez-Palenzuela, F. Centellas, J. A. Garrido, C. Arias, R. M. Rodríguez, E. Brillas and P. L. Cabot, *J. Power Sources*, 2011, **196**, 3503–3512.
40 S. N. Azizi, S. Ghasemi and F. Amiripour, *Electrochim. Acta*, 2014, **137**, 395–403.
41 N. Y. Sreedhar, M. Sunil Kumar and K. Krishnaveni, *Sens. Actuators, B*, 2015, **210**, 475–482.
42 D. K. Gosser, *Cyclic voltammetry: simulation and analysis of reaction mechanisms*, VCH Publishers, New York, 1993.
43 E. Telli, A. Döner and G. Kardaş, *Electrochim. Acta*, 2013, **107**, 216–224.
44 M. Wang, Y. W. He, R. X. Li, Z. Z. Ma, Z. H. Zhang and X. G. Wang, *Electrochim. Acta*, 2015, **178**, 259–269.
45 W. Q. Gao, Q. L. Liu, X. L. Zhao, C. Cui, S. Zhang, W. J. Zhou, X. N. Wang, S. H. Wang, H. Liu and Y. H. Sang, *Nano Energy*, 2021, **80**, 105543.
46 T. E. R. Fiuza and D. Zanchet, *ACS Appl. Nano Mater.*, 2020, **3**, 923–934.
47 K. C. Shen, H. T. Sun, K. Q. Li, G. H. Liang, Q. T. Gong, Z. C. Yan, K. Kim and W. M. Wang, *J. Alloys Compd.*, 2021, **863**, 158080.
48 C. X. Wang, L. Xu, X. W. Xu, H. Cheng, H. C. Sun, Q. Lin and C. Zhang, *J. Colloid Interface Sci.*, 2014, **416**, 274–279.
49 I. Sobczak and Ł. Wolski, *Catal. Today*, 2015, **254**, 72–82.
50 C. H. Tsai, S. Y. Chen, J. M. Song, I. G. Chen and H. Y. Lee, *Corros. Sci.*, 2013, **74**, 123–129.
51 O. Arbeláez, T. R. Reina, S. Ivanova, F. Bustamante, A. L. Villa, M. A. Centeno and J. A. Odriozola, *Appl. Catal., A*, 2015, **497**, 1–9.
52 B. Hammer and J. K. Nørskov, *Adv. Catal.*, 2000, **45**, 71–129.
53 S. Jalili, A. Z. Isfahani and R. Habibpour, *Comput. Theor. Chem.*, 2012, **989**, 18–26.
54 Z. L. Wang, S. C. Ning, P. Liu, Y. Ding, A. Hirata, T. Fujita and M. W. Chen, *Adv. Mater.*, 2017, **29**, 1703601.
55 J. M. Hermann, H. Müller, L. Daccache, C. Adler, S. Keller, M. Metzler, T. Jacob and L. A. Kibler, *Electrochim. Acta*, 2021, **388**, 138547.
56 R. Seakr, *Trans. Nonferrous Met. Soc. China*, 2017, **27**, 1423–1430.
57 Y. Q. Wang, W. Tang and L. Zhang, *J. Mater. Sci. Technol.*, 2015, **31**, 175–181.
58 B. Liu, P. Eisenlohr, F. Roters and D. Raabe, *Acta Mater.*, 2012, **60**, 5380–5390.
59 Y. L. Lu, R. Chen, Y. F. Wang and Z. Chen, *Phys. B*, 2021, **622**, 413363.
60 N. Xu, L. Chen, B. K. Gu, Z. K. Ren, Q. N. Song and Y. F. Bao, *Trans. Nonferrous Met. Soc. China*, 2021, **31**, 3785–3799.
61 Y. Fang and X. Q. Gong, *Chin. Chem. Lett.*, 2019, **30**, 1346–1350.
62 Y. Lee, A. Loew and S. H. Sun, *Chem. Mater.*, 2010, **22**, 755–761.
63 W. K. Chen, S. H. Liu, M. J. Cao, Q. G. Yan and C. H. Lu, *J. Mol. Struct.: THEOCHEM*, 2006, **770**, 87–91.